Seismic singularities at upper-mantle phase transitions: a site percolation model

Felix J. Herrmann[1] and Yves Bernabé[2]

[1]*Department of Earth and Ocean Sciences, The University of British Columbia, Vancouver, BC V6T 1Z4, Canada. E-mail: fherrmann@eos.ubc.ca*
[2]*Department of Earth, Atmospheric and Planetary Sciences, Massachusetts Institute of Technology, Cambridge, MA, USA*

SUMMARY

Mineralogical phase transitions are usually invoked to account for the sharpness of globally observed upper-mantle seismic discontinuities. We propose a percolation-based model for the elastic properties of the phase mixture in the coexistence regions associated with these transitions. The major consequence of the model is that the elastic moduli (but not the density) display a singularity at the percolation threshold of the high-pressure phase. This model not only explains the sharp but continuous change in seismic velocities across the phase transition, but also predicts its abruptness and scale invariance, which are characterized by a non-integral scale exponent. Using the receiver-function approach and new, powerful signal-processing techniques, we quantitatively determine the singularity exponent from recordings of converted seismic waves at two Australian stations (CAN and WRAB). Using the estimated values, we construct velocity–depth profiles across the singularities and verify that the calculated converted waveforms match the observations under CAN. Finally, we point out a series of additional predictions that may provide new insights into the physics and fine structure of the upper-mantle transition zone.

Key words: percolation, phase transition, seismology, transition zone, upper mantle, waveform analysis.

1 INTRODUCTION

Analysis of global seismological data reveals that the seismic properties of mantle material change abruptly at 410- and 660-km depths (for example from *P*-to-*S* converted waves, Paulssen 1988; Gurrola & Minster 1998; Chevrot *et al.* 1999; *SH*-polarized reverberations, Revenaugh & Jordan 1991; stacked long-period data, Shearer 1990; Shearer & Flanagan 1999; precursors to *SS*, Gu *et al.* 1997; and precursors to *P'P'*, Xu *et al.* 2003). The 410- and 660-km seismic discontinuities are attributed to mineral iso-compositional phase transitions experimentally observed to be sharp, namely the olivine to β-spinel and the γ-spinel to perovskite+magnesiowüstite transitions (e.g. Anderson 1989; Bina 1991; Helffrich & Wood 2002; see also Petersen *et al.* 1993; Gaherty *et al.* 1999; Weidner & Wang 2000; Lebedev *et al.* 2002; Xu *et al.* 2003). The discontinuities are situated near the ends of the transition zone, a broad region of the mantle characterized by velocity gradients steeper than those arising from the pressure dependence of the elastic constants and density of the minerals (e.g. Dziewonski & Anderson 1981; Anderson 1989; Karki *et al.* 2001; Sinogeikin & Bass 2002). These anomalous gradients are attributed to the gradual eclogite to garnetite transition, possibly followed by transformation of garnet-majorite to perovskite (e.g. Anderson 1989; Bina 1991; Weidner & Wang 2000; Helffrich & Wood 2002). It is thought that homogeneous mixing (for example solid solution) of the two phases can only produce gradually

varying elastic properties (e.g. Bina & Wood 1984; Akaogi *et al.* 1987). However, we argue that singularities in the elastic properties (i.e. points where the derivative diverges) must arise at depths where the strong, high-pressure phases become connected, if the mixing is heterogeneous (owing, for example, to random formation of macroscopic inclusions; e.g. Perlovsky 1991). As we will show in this paper, frequency-dependent conversion and reflection of elastic waves occur at these singularities (see also Perlovsky 1986, 1991), leading to an alternative explanation of the global seismological data mentioned above.

For two stations in Australia, our conceptual model is corroborated by a receiver-function study and subsequent waveform modelling. Indeed, we found that the imaged waveforms obtained from the seismic data were consistent with the leading-order amplitude behaviour predicted by the percolation model. Here, the term 'leading-order behaviour' refers to the robust, low-frequency characteristics of the waveforms. Differences in arrival times due to possible strong lateral velocity and thickness variations of the transition zone (e.g. Grand *et al.* 1997), albeit important, are not of primary concern in this paper. Instead, our primary goal is to show that the percolation model predicts waveforms that, to leading order, can be reconciled with observations for these stations, irrespective of possible image deterioration due to azimuthal dependence, lateral velocity and thickness variations, which mainly influence the high frequencies.
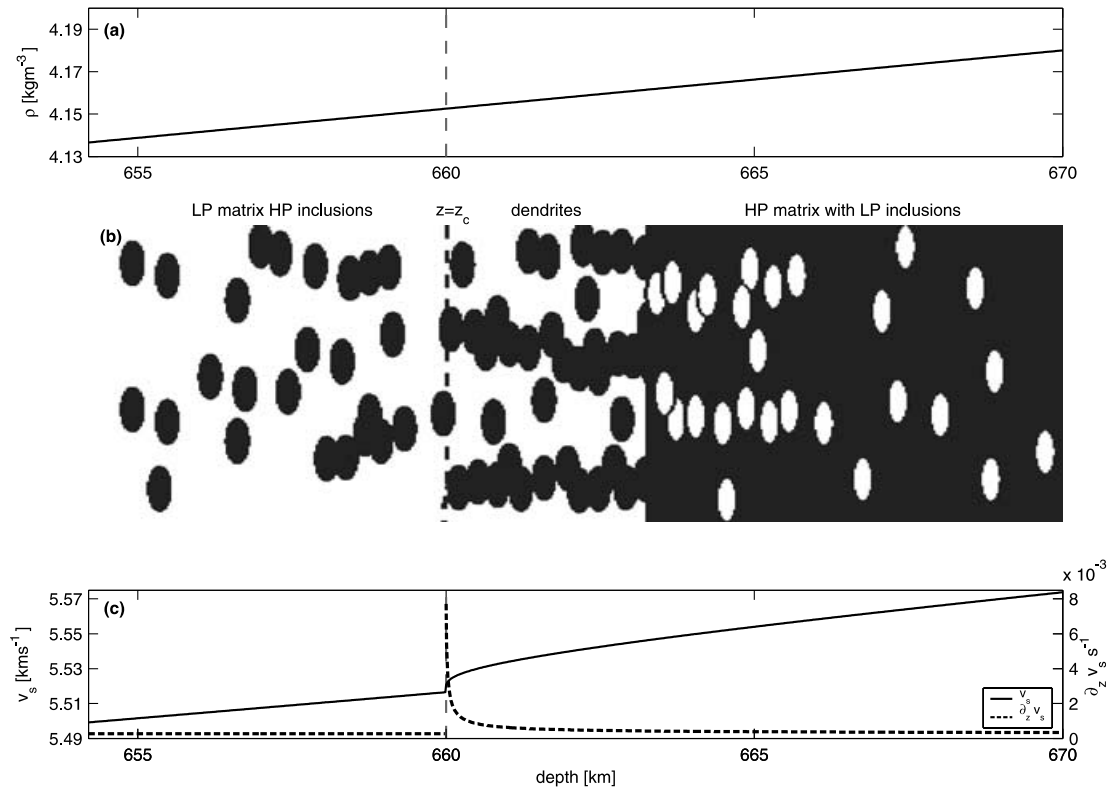
GJI Seismology

Figure 1. Site percolation model (SPM) of the coexistence region. (a) Depth profile of the mixture density, $\rho = q\rho_{LP} + p\rho_{HP}$, which does not behave singularly for a smoothly varying composition, $p(z)$. (b) Schematic illustration of the phase transition by formation of high-pressure (HP) phase inclusions in a low-pressure (LP) matrix. The HP inclusions (black) are assumed to be horizontally oriented ellipsoids. At the critical depth z_c (dotted line) the HP inclusions percolate, form an infinite cluster containing long vertical dendrites of LP matrix and some isolated HP inclusions. (c) Corresponding shear wavespeed profile (solid line) showing a singularity at z_c. The singularity is clearly apparent in the derivative (dashed line). The magnitude of the singularity depends on the difference between the mixing laws (here Reuss and Voigt averages). The value for the singularity order was taken to be $\beta = 0.30$, corresponding to the estimated value for the 410-km discontinuity under CAN. Although the pressure dependence is included here, the overall gradient is due to phase mixing over a wide coexistence region and is consistent with anomalous gradients observed in the transition zone (Anderson 1989; Sinogeikin & Bass 2002).

The paper is organized as follows. First, we present the site percolation model. Second, we characterize the leading-order behaviour of converted waveforms at the singularities for two Australian stations. We then compare the seismic observations with predictions of the percolation model. We finish with a discussion of the implications of our model.

2 SITE PERCOLATION MODEL OF THE CO-EXISTENCE REGIONS

Although the mineralogy of the Earth's mantle is likely to be complex, especially around the 410- and 660-km phase transitions (e.g. Anderson 1989; Bina 1991; Helffrich & Wood 2002), we will assume that, as far as modelling of the elastic properties is concerned, we can use a simplified two-phase model with volume fractions that depend on the vertical coordinate only. For each of the phase transitions mentioned above, we consider the region where both of the mineralogical phases involved in the phase transition coexist (see Fig. 1b). At the top of the coexistence region, the material consists exclusively of the low-pressure (LP) phase. With increasing depth, inclusions of the high-pressure (HP) phase are progressively formed until only HP material remains. For the sake of simplicity, we assume that the volume fractions of HP and LP material, p and $q = 1 - p$, are linear functions of depth z (see Fig. 1a). This assumption is non-essential, however, and more complicated but smoothly

varying functions of z can be used. At a critical depth z_c, which corresponds to the percolation threshold $p_c = p(z_c)$ and is denoted by the vertical dashed lines in Fig. 1, an 'infinite', connected HP cluster is formed (we assume that finite-size analysis is unnecessary here). It is important to note that, for $z \geq z_c$, not all HP inclusions belong to the infinite cluster. Isolated HP inclusions can still be found, embedded in the remaining LP material and forming with it a mixture (M). In summary, above z_c we have a weak LP matrix containing randomly distributed, non-percolating, strong HP inclusions. Below z_c, a strong HP skeleton is intertwined with the weaker mixed material M.

Percolation theory predicts that, in the vicinity of the percolation threshold, the volume fraction p^* of HP material that belongs to the infinite cluster is zero for $p < p_c$ (i.e. above z_c) and has a power-law dependence on $(p - p_c)$ for $p \geq p_c$ (Stauffer & Aharony 1992). For convenience, we assume that this power law extends all the way to the bottom of the coexistence region (i.e. $p = 1$). Hence, p^* is given by

$$p^* = p \left(\frac{p - p_c}{1 - p_c} \right)^{\beta}, \tag{1}$$

where the exponent β is a positive real number, which, in general, is considered to be 'universal' (i.e. it depends only on spatial dimensionality, not, for example, on the interconnection topology of the inclusions). Site percolation theory predicts $\beta = 0.41$

in 3-D discrete lattices in the case of an isotropic, δ-correlated, stochastic process (Stauffer & Aharony 1992). However, universality of the percolation exponents is unlikely to hold in the case of the mantle phase transitions. Indeed, the stochastic process responsible for inclusion emplacement should presumably display long-range, possibly anisotropic, spatial correlation owing to the elastic interaction of an inclusion with its surroundings (Kaganova & Roitburd 1988). This causes a change of the exponent β, especially since the inclusion connectivity problem belongs to continuum rather than lattice percolation (e.g. Isichenko 1992; Sahimi & Mukhopadhyay 1996). Consequently, we must follow an empirical approach and use seismic data to constrain β for the 410- and 660-km singularities, assuming that these depths correspond to z_c in both cases.

Below z_c, the volume fraction of the mixed material M is, of course, given by $q^* = (1 - p^*)$. To model M, we need the volume fractions of its LP and HP parts, $q_M = (1 - p)/\{(1 - p) + (p - p*)\}$ and $p_M = (1 - q_M)$, respectively. A simple calculation yields

$$p_M = 1 - \frac{q}{1 - p\left(\frac{p - p_c}{1 - p_c}\right)^{\beta}}. \tag{2}$$

It is well known in solid-state physics and mechanical engineering that a binary mixture is elastically strong if its strong component forms a connected cluster, and weak otherwise (e.g. Ledbetter *et al.* 1984; Gai *et al.* 1984; Deptuck *et al.* 1985; Turusov *et al.* 1986; Marion & Nur 1989; Favier *et al.* 1997; Novikov *et al.* 2001; for other applications of percolation theory to mechanics, see de Gennes 1976, or Roux & Guyon 1985). Thus a realistic elastic model of the coexistence region must take into account the connectivity (or lack of connectivity) of the HP phase.

We begin by assuming that both the HP and LP phases are elastically isotropic and that the HP inclusions have a spherical shape so that the HP/LP mixture is locally (statistically) isotropic as well. Hashin & Shtrikman (1962) demonstrated that the elastic moduli of statistically isotropic binary mixtures are tightly bounded by two quantities known as the Hashin–Shtrikman (HS) bounds. More importantly, it has been shown that the HS bounds can effectively be used to model the elastic properties of materials consisting of isolated spherical inclusions randomly distributed inside a continuous (connected) matrix (e.g. Mori & Tanaka 1973; Benveniste 1987), even for non-dilute concentrations of inclusions (e.g. Luo & Weng 1987). Note that the model accuracy increases with decreasing elastic contrast between the two components of the mixture. The upper HS bound must be used when the strong component forms the connected matrix, while the lower one applies otherwise (e.g. Marion & Nur 1989; Favier *et al.* 1997; Novikov *et al.* 2001; Saidi *et al.* 2003). Accordingly, the bulk modulus K of the coexistence region above z_c is given by the lower HS bound:

$$K = K_{LP}\left(1 + \frac{p(K_{HP} - K_{LP})}{q(K_{HP} - K_{LP})a_{LP} + K_{LP}}\right), \tag{3}$$

where $a_{LP} = 3\,K_{LP}/(3\,K_{LP} + 4\,G_{LP})$ and the subscripts LP and HP refer to the mineralogical phases involved in the phase transition. A similar relation is obtained for the shear modulus G, except that a_{LP} is replaced by

$$b_{LP} = 6\,(K_{LP} + 2\,G_{LP})/5(3\,K_{LP} + G_{LP}).$$

Below z_c we must switch to the higher HS bound:

$$K = K_{HP}\left(1 + \frac{q^*(K_M - K_{HP})}{p^*(K_M - K_{HP})a_{HP} + K_{HP}}\right), \tag{4}$$

where K_M is the bulk modulus of the mixed material M. Since the HP inclusions in M are isolated, K_M is calculated using the lower HS bound:

$$K_M = K_{LP}\left(1 + \frac{p_M(K_{HP} - K_{LP})}{q_M(K_{HP} - K_{LP})a_{LP} + K_{LP}}\right). \tag{5}$$

Similar equations can be written for G, replacing a_{LP} and a_{HP} by b_{LP} and b_{HP}. Hence, we can calculate K and G for all values of p between 0 and 1. One major consequence of this model is that it predicts a β-order singularity in the elastic moduli as the critical depth z_c is approached from below (instead of a zero-order jump or first-order ramp discontinuity as assumed in current models). This is illustrated in Fig. 2(a), where three examples corresponding to $\beta = 0.23$, 0.41 and 0.65 are shown. We used a Poisson's ratio of 0.3 and a 10-fold increase between K_{LP} and K_{HP}. This very large contrast in elastic properties is not appropriate for the Earth's mantle but was used here to enable the singularity to be visualized by increasing the difference between the upper and lower HS bounds. It is clear, however, that the singularity persists even for vanishing elastic contrasts between the LP and HP phases. This is demonstrated in Fig. 2(b), which shows the first derivative dK/dp as a function of p for a 10 per cent contrast in K. One consequence of this model is that, although the mixture density, $\rho = q\rho_{LP} + p\,\rho_{HP}$, does not behave singularly (see Figs 1 and 8), the P- and S-wave velocities, $V_P = [(K + 4G/3)/\rho\,]^{1/2}$ and $V_S = [G/\rho\,]^{1/2}$, do. Note also that the variations of the LP and HP properties with depth (owing to their dependence on pressure and temperature) can be easily included in the model by considering all the LP and HP parameters as functions of z, i.e. $K_{LP}(z)$, $K_{HP}(z)$, $G_{LP}(z)$, $G_{HP}(z)$, $\rho_{LP}(z)$ and $\rho_{HP}(z)$.

Because the elastic contrasts between the LP and HP minerals at the 410- and 660-km transitions are small, however, the HS bounds are nearly coincident and therefore lead to converted phases with amplitudes too small compared with seismic observations. One possible solution is to discard the isotropy assumption and consider horizontally oriented, oblate ellipsoidal inclusions (consistent with thermodynamic equilibrium, Kaganova & Roitburd 1988), which hypothetically coalesce below z_c into long, vertical dendrites, leaving prolate M inclusions between them (see Fig. 1b). This leads to a transversely isotropic structure (with a vertical symmetry axis) both above and below z_c. For any value of the aspect ratio (i.e. the minor to major axis ratio) of the inclusions, we calculate Eshelby's tensor $\boldsymbol{S}$ (Eshelby 1957; Mura 1982) and apply Mori–Tanaka's method (Mori & Tanaka 1973; Benveniste 1987; Schjodt-Thomsen & Pyrz 2001) to obtain the stiffness tensor $\boldsymbol{C}$ above and below z_c. For $z < z_c$, we have

$$\boldsymbol{C} = \boldsymbol{C}_{LP} + p(\boldsymbol{C}_{HP} - \boldsymbol{C}_{LP}) \cdot \boldsymbol{T}_{LP} \cdot (q\boldsymbol{I} + p\boldsymbol{T}_{LP})^{-1}, \tag{6}$$

where $\boldsymbol{I}$ is the unit tensor, $\boldsymbol{C}_{LP}$ and $\boldsymbol{C}_{HP}$ the isotropic stiffness tensors for the LP and HP phases, $\boldsymbol{T}_{LP}$ the inverse of $[\boldsymbol{I} + \boldsymbol{S} \cdot \boldsymbol{C}_{LP}^{-1} \cdot (\boldsymbol{C}_{HP} - \boldsymbol{C}_{LP})]$ and the dots refer to tensor products. Note that, here, $\boldsymbol{S}$ is Eshelby's tensor for an oblate HP inclusion embedded in a LP matrix. For $z \geq z_c$, the relation becomes

$$\boldsymbol{C} = \boldsymbol{C}_{HP} + q^*(\boldsymbol{C}_M - \boldsymbol{C}_{HP}) \cdot \boldsymbol{T}_M \cdot (p^*\boldsymbol{I} + q^*\boldsymbol{T}_{HP})^{-1}, \tag{7}$$

where $\boldsymbol{T}_M$ is the inverse of $[\boldsymbol{I} + \boldsymbol{S} \cdot \boldsymbol{C}_{HP}^{-1} \cdot (\boldsymbol{C}_M - \boldsymbol{C}_{HP})]$. Now $\boldsymbol{S}$ is Eshelby's tensor for a prolate M inclusion embedded in a HP matrix. The stiffness tensor of the mixed material M is given by

$$\boldsymbol{C}_M = \boldsymbol{C}_{LP} + p_M(\boldsymbol{C}_{HP} - \boldsymbol{C}_{LP}) \cdot \boldsymbol{T}_{LP} \cdot (q_M\boldsymbol{I} + p_M\boldsymbol{T}_{LP})^{-1}. \tag{8}$$

Note that eqs (6)–(8) reduce to eqs (3)–(5) for K, and their equivalent for G, when the inclusions are spherical.
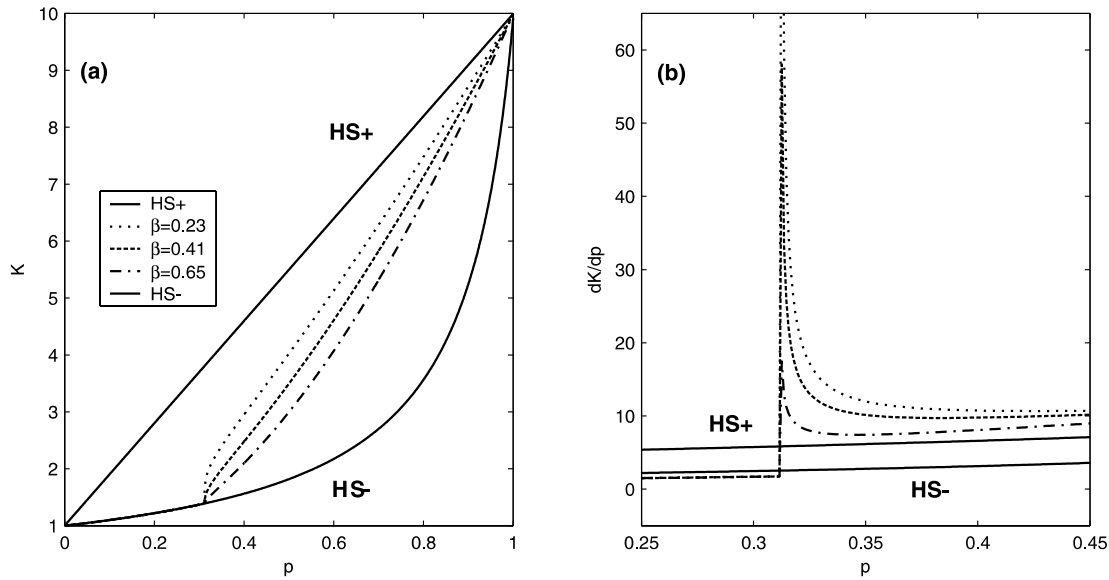
Figure 2. Illustration of the singularity predicted by the SPM for the exponent $\beta = 0.23$, 0.41 and 0.65 (assuming a single Poisson ratio of 0.3). (a) Mixture curves for a 10-fold contrast in K (in different dashings) and the lower and upper HS bounds (solid lines). Notice the onset-like singularity at the critical point, $p_c = 0.32$, where the connected cluster is formed. As the exponent decreases the onsets become sharper. (b) Curves of the first derivative dK/dp for a 10 per cent contrast in K (in colour) and the smooth first derivative of the lower and upper HS bounds as a function of p (in black). The singularity is located at the point at which the compressibility profile 'jumps' from the lower HS bound to the higher. Even though the contrast in K is only 10 per cent, the first derivative, which is proportional to the P-to-S conversion coefficient, shows large variations.

We can finally calculate the elastic wave velocities as a function of the aspect ratio and incidence angle (Thomsen 1986). We tested these calculations and found that, near normal incidence, V_P and V_S asymptotically approach limiting values as the aspect ratio is decreased to zero (corresponding to the largest possible anisotropy). These limiting values can be equivalently computed by replacing the lower and higher HS bounds in eqs (3)–(5) by Reuss and Voigt averages (indeed, the Reuss average corresponds to *in series* arrangements of the phases while the Voigt average applies to *in parallel* configurations):

$$K = \left(\frac{q}{K_{LP}} + \frac{p}{K_{HP}} \right)^{-1} \qquad \text{(for } z < z_c\text{),} \tag{9}$$

$$K = q^* K_M + p^* K_{HP} \qquad \text{(for } z \geq z_c\text{)} \tag{10}$$

and

$$K_M = \left(\frac{q_M}{K_{LP}} + \frac{p_M}{K_{HP}} \right)^{-1}. \tag{11}$$

Notice that eqs (9)–(11) are accurate to about 1/1000 for aspect ratios as large as 1/10. We verified that, using eqs (9)–(11), the separation between the upper and lower mixing curves was greater than that obtained with eqs (3)–(5) using identical parameters. Since eqs (9)–(11) are much easier to implement than the tensor equations (6)–(8), we will use them in our forward modelling of the converted waves in Section 4.

Finally, note that the vertical extent of the coexistence regions cannot be derived from percolation theory but may be inferred from independent evidence (for example from observed abnormal gradients or from experimental mineralogy data).

3 SEISMIC IMAGING, CHARACTERIZATION AND DETECTION OF SINGULARITIES

The major consequence of the percolation model is that it predicts a β-order singularity in the elastic bulk moduli as the critical depth z_c is approached from below. Thus, the fluctuations in the elastic bulk moduli with respect to a smoothly varying background obey the following power-law relation:

$$\Delta(z) \propto \begin{cases} (z - z_c)^\beta & z \geq z_c \\ 0 & z < z_c \end{cases} \quad \text{with} \quad 0 < \beta < 1, \tag{12}$$

where the symbol Δ refers to fluctuations in the bulk modulus, $\Delta K = (K - \bar{K})/\bar{K}$, or shear modulus, $\Delta G = (G - \bar{G})/\bar{G}$, with the barred quantities representing (moving) averages such that ΔK, $\Delta G \ll 1$. Notice that eq. (12) implies divergence of the α-order derivative at $z = z_c$ (with $\alpha > \beta$). Conversely, the mineralogy, as expressed by the volume fractions (p and q) and the mixture density ($\rho = q\rho_{LP} + p\rho_{HP}$), varies smoothly. Since β cannot be theoretically constrained, we must instead use seismic waves to probe the singularity and estimate the exponent.

Non-integral-order singularities (see eq. 12) differ in several respects from the first- or higher-integer-order singularities, which are used in current seismic-discontinuity models and include a characteristic length scale, i.e. a thickness (see e.g. Paulssen 1988; Gaherty *et al.* 1999; Xu *et al.* 2003). This characteristic length scale marks a cross-over between a relatively smooth behaviour for the small wavelengths (i.e. $\beta = 1$) to a discontinuous behaviour for the large wavelengths (i.e. $\beta = 0$). Non-integral singularities of the above type are scale-invariant (i.e. no cross-over occurs and, consequently, the fluctuations in the compressional/shear modulus are invariant with respect to scale dilatations/compressions). The scale invariance is expressed by $\Delta(z) = r^{-\beta} \Delta(rz)$ for $r > 0$ (i.e. a dilatation for $r > 1$ and a compression for $0 < r < 1$). It gives rise to seismic reflections and mode conversions that change the waveform,

irrespective of the dominant seismic wavelength/scale. For $\beta <$ 1, these singularities are sharper then first- or higher-order discontinuities (Herrmann *et al.* 2001; Herrmann 2001), and consequently yield relatively stronger reflections and mode conversions for similar velocity contrasts. The exponent β controls the transition abruptness and the leading-order behaviour of the associated waveforms (see Fig. 5), i.e. the scaling and, hence, the frequency-dependent amplitudes of the converted phases. It thus provides a parametrization for modelling the mantle phase transitions that goes beyond the currently assumed integer-order seismic discontinuities.

Using a receiver-function approach (Paulssen 1988; Petersen *et al.* 1993; Gurrola & Minster 1998; Chevrot *et al.* 1999) supplemented by an imaging condition, we can characterize the leading-order behaviour of the depth-imaged *P*-to-*S* transmission coefficient (i.e. from the *Pds* phases) and gain access to the shape of the singularity, i.e. its order. In the ideal case of an infinite seismic bandwidth and dispersion-free medium, the singularity order could be estimated by measuring the scaling properties, for example by using the continuous wavelet transform (Mallat 2000). In seismic imaging, the wavelet transform corresponds to measuring the mode conversion as a function of the central frequency of the source-time function. Unfortunately, seismic data are bandwidth-limited due to the fixed nature of the source-time function and possible dispersion mechanisms along the ray paths. We rule out dispersion as the prime process responsible for the distortion of the converted waveforms for two reasons. First, we assume that there are no significant differences between the dispersion properties of the *P* and *S* waves along the ray path from the upper-mantle discontinuities to the surface. In that case, the deconvolution for the observed *P* wave remains effective in removing the dispersion effects from the converted waveform. Second, for relatively low frequencies, dispersion-induced waveform distortions are of smaller order than the leading-order waveform distortion induced by the shape of the singularity. Using a similar argument, we ignore possible loss in coherence in our stacking procedure resulting from azimuthal dependence of the traveltimes, lateral velocity variations and possible topography within the Fresnel zone.

Instead of using the multiscale wavelet-transform analysing technique, we use the principle of matched filtering from signal-detection theory to deal with the bandwidth limitation and the presence of noise. We correlate the noisy bandwidth-limited image with a template of parametrized waveforms and find those waveforms that maximize the correlation (Mallat 2000) between converted events and elements of our parametrized template list (or dictionary). Using the greedy search algorithm called Matching Pursuit (Mallat 2000), we obtain estimates for the amplitude, location, dominant wavelength and order of the singularity. To establish whether the percolation model captures the observed seismic waveform distortions, we apply the imaging and singularity characterization techniques mentioned above to data from two high-quality Australian stations (both were ranked 1 in Table 1 of Chevrot *et al.* 1999, indicating the highest quality), CAN (geoscope) and WRAB (IRIS): see Fig. 3 for maps and further details of the selected events.

3.1 Seismic imaging method

Receiver-function data are used to image observed *Pds* converted phases (i.e. up-going compressional *P* waves that convert at discontinuities, *d*, and propagate towards the surface as shear *S* waves, *s*).

These phases are commonly used in receiver-function imaging (see e.g. Chevrot *et al.* 1999), because, to leading order, the transmitted *P* waves do not see the transitions while the *P*-to-*S* converted waves are sensitive to the detailed shape of the singularities. As a consequence, *P* waves at the surface (*Pdp* phases) mainly contain contributions from the source-time and Green's functions along the ray path, except for the relatively short ray path from the conversion point, *d*, to the surface along which a shear wave also travels. For not too large differences in amplitude behaviour for the compressional and shear Green's functions, the *Pdp* recordings can be used to deconvolve the source-time and Green's function. This approach has successfully been applied in imaging upper-mantle discontinuities (Paulssen 1988; Petersen *et al.* 1993; Gurrola & Minster 1998; Chevrot *et al.* 1999). To facilitate the interpretation of the imaged waveforms, we propose a modified imaging scheme that (1) aims to preserve as much of the frequency content as possible, using non-linear edge-preserving estimation techniques borrowed from theoretical signal processing (Donoho & Johnstone 1998; Mallat 2000; Abramovich & Silverman 1998; Neelamani *et al.* 2004), and (2), by imposing an imaging condition (Claerbout 1971), provides depth images rather then images as a function of the differential traveltime with respect to the *P* arrival. This imaging condition only considers events arriving at $t = 0$, is applied on the inversely extrapolated, moveout-corrected converted wavefield, and differs from after-stack traveltime–depth conversion. Our scheme consists of the following steps.

(1) **Pre-processing.** Individual *Pdp* phases (i.e. up-going compressional *P* waves transmitted through the discontinuity, *d*, and propagating to the surface as compressional waves, *p*) from different events are sorted as a function of the ray parameter, aligned with respect to the direct *P* arrival and rotated in their polarization axis using the method proposed by Chevrot *et al.* (1999). As stated earlier, we are interested in the low-frequency, leading-order behaviour and, therefore, ignore the azimuthal dependence. As can be seen from Fig. 3, most of the events for CAN are clustered around northwestern directions, while the data for WRAB may be more influenced by azimuthal differences.

(2) **Deconvolution.** For each trace, a window is selected that contains the reference pulse given by the *Pdp* phases. The converted *Pds* phases are deconvolved by regularized spectral division (i.e. a regularized least-squares formulation of the deconvolution problem for each event separately) using the windowed reference pulses. To minimize the distortion, we use a regularization parameter/water level as small as possible in conjunction with a non-linear wavelet-estimation technique known as ForWaRD (Donoho & Johnstone 1998; Mallat 2000; Neelamani *et al.* 2004), which removes the noise after spectral division by wavelet thresholding. After deconvolution we can express the ray-parameter-dependent reference pulses, $P(z = 0; t, p)$, and converted phases, $Q(z = 0; t, p)$, at the surface, respectively, by

$$\mathbf{decon} : Pdp(p) \Rightarrow P(z = 0; t, p) = \varphi_t^{\text{residual}}(t, p) \propto \delta(t),$$
$$\mathbf{decon} : Pds(p) \Rightarrow Q(z = 0; t, p) \tag{13}$$

where $\delta(t)$ denotes the Dirac delta distribution, the time t is measured with respect to the *P* arrival, and p is the ray parameter in spherical coordinates (notice that, in the present context, p refers to the ray parameter and not to the volume fraction). The symbol $\varphi_t^{\text{residual}}(t, p)$ is used to describe the residual delta-like waveform that remains after deconvolution. This residual is due to regularization and to constraints on the bandwidth. It expresses the effective
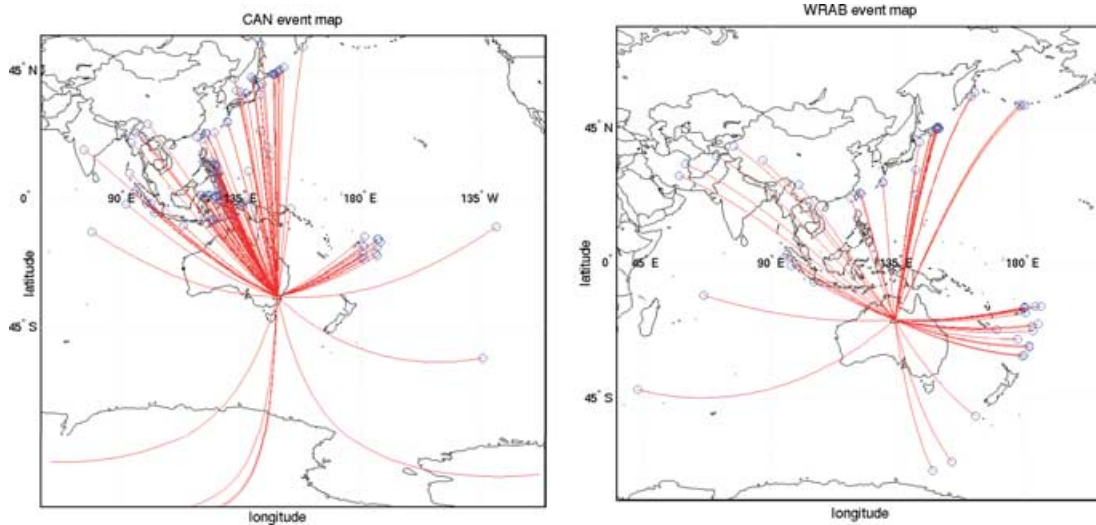
Figure 3. Event maps for the two stations considered in the paper. Only events larger then magnitude 5.5 were considered. The data were binned (we stacked over the azimuth) for various slownesses. The CAN data consisted of 125 events with slownesses in the range [4.67–8.71] s per degree. The WRAB data consisted of 56 events with slownesses in the range [4.70–8.80] s per degree. For the periods we are operating at, the Fresnel zones have a radius of 100 to 150 km (Chevrot *et al.* 1999; Cox 2002).

resolution with which the *P* wave illuminates the transition from below.

(3) **Inverse extrapolation.** We use the IASPEI91 velocity model (Kennett & Engdahl 1991) to calculate the differential traveltime, expressing the arrival time difference between the *Pdp* and the *Pds* phases. These traveltimes (see e.g. Gurrola & Minster 1998; Chevrot *et al.* 1999) are given by

$$T_{ps}(p, z) = \int_0^z [\sqrt{\bar{v}_s^{-2}(z') - p^2(z')} - \sqrt{\bar{v}_p^{-2}(z') - p^2(z')}]dz', \quad (14)$$

where the reference ray parameter, $p(z) = \deg \times 180[\pi(6371 - z)]$, is in spherical coordinates, the slowness, p is in s deg^{-1}, and the smoothed reference compressional and shear wavespeeds, $\bar{v}_p, \bar{v}_s$, are derived from the IASPEI91 model. We use the bar to distinguish these smoothed velocities from the singular velocity profiles predicted by the percolation model. With these traveltimes, we inversely extrapolate and moveout-correct the converted phases from the surface down to depth level z according to

extrapol. : $Q(z = 0; t, p) \Rightarrow Q(z, t, p)$
$$= (Q(z = 0; \cdot, p) * \delta(\cdot - \Delta T_{ps}(p, z)))(t), \quad (15)$$

where the symbols $*$ and $\cdot$ respectively denote convolution and the variable over which the convolution integral is calculated.

(4) **Depth imaging.** To capture the main contribution from the conversion point at depth, we apply an imaging condition (Claerbout 1971). This condition corresponds to the estimated amplitude of the inversely extrapolated and deconvolved converted phases evaluated at $t = 0$:

$$Q(z; t, p) \Rightarrow \hat{t}_{ps}(z, p) = Q(z, t = 0, p) = \Re \int_0^\infty$$
$$\breve{Q}(z; \omega)d\omega, \quad (16)$$

where $\breve{Q}(z; \omega)$ is the temporal Fourier transform of $Q(z; \omega)$ and $\hat{t}_{ps}(z, p)$ represents the estimated ray parameter and depth-dependent *P*-to-*S* transmission coefficient.

(5) **Stacking.** Because of limitations in the signal-to-noise ratio, limited ray-parameter aperture, and the insensitivity of the *P*-to-*S*

transmission coefficient to fluctuations in density, we apply a stacking procedure rather than inversion (weighted stack):

$$\hat{t}_{ps}(z, p) \Rightarrow \hat{t}_{ps}^{\text{stacked}}(z) = \frac{1}{\#p} \sum_{i=1}^{\#p} \hat{t}_{ps}(z, p_i). \quad (17)$$

This stacking procedure preserves the leading-order low-frequency behaviour of the waveform but may lead to some loss of coherence for the high frequencies due to misalignments caused by azimuthal dependence and/or topography and strong lateral velocity variations.

By applying the above steps, we arrive at leading-order estimates for depth images of the waveforms of the *P*-to-*S* mode conversions at the upper-mantle discontinuities with reasonable signal-to-noise ratios and resolution. Note, however, that the bootstrap error bars appear to be relatively large.

The imaging procedure described above also leads to an approximate forward model for the imaged waveforms, where the fluctuations in the shear modulus are directly related to the waveforms via a spatial convolution,

$$t_{ps}^{\text{stacked}}(z) \approx \frac{d}{dz} \left(\Delta G * \varphi_z^{\text{residual}} \right)(z), \quad (18)$$

where the depth-parametrized residual 'source-time' function, $\varphi^{\text{residual}}$, is related to the remaining delta-like waveform for the stacked deconvolved *P* waves incident from below, and ΔG represents the fluctuations in the shear modulus. From this point on, we will reserve the symbols $t_{ps}(z)$ and $\hat{t}_{ps}(z)$ for the (stacked and imaged) transmission coefficients. The problem is then reduced to finding the Δs that minimize the difference between model and observations, given estimates for the residual source-time functions (interpreted as vertical resolution/scaling functions).

In Fig. 4 we show images of the 410- and 660-km singularities under CAN and WRAB, computed using the above imaging scheme. To improve the signal-to-noise ratio and to obtain more coherent images for the upper-mantle transitions, noise caused by misalignments is suppressed by low-pass filtering. Low-pass filtering does not influence the low-frequency part of the spectrum,
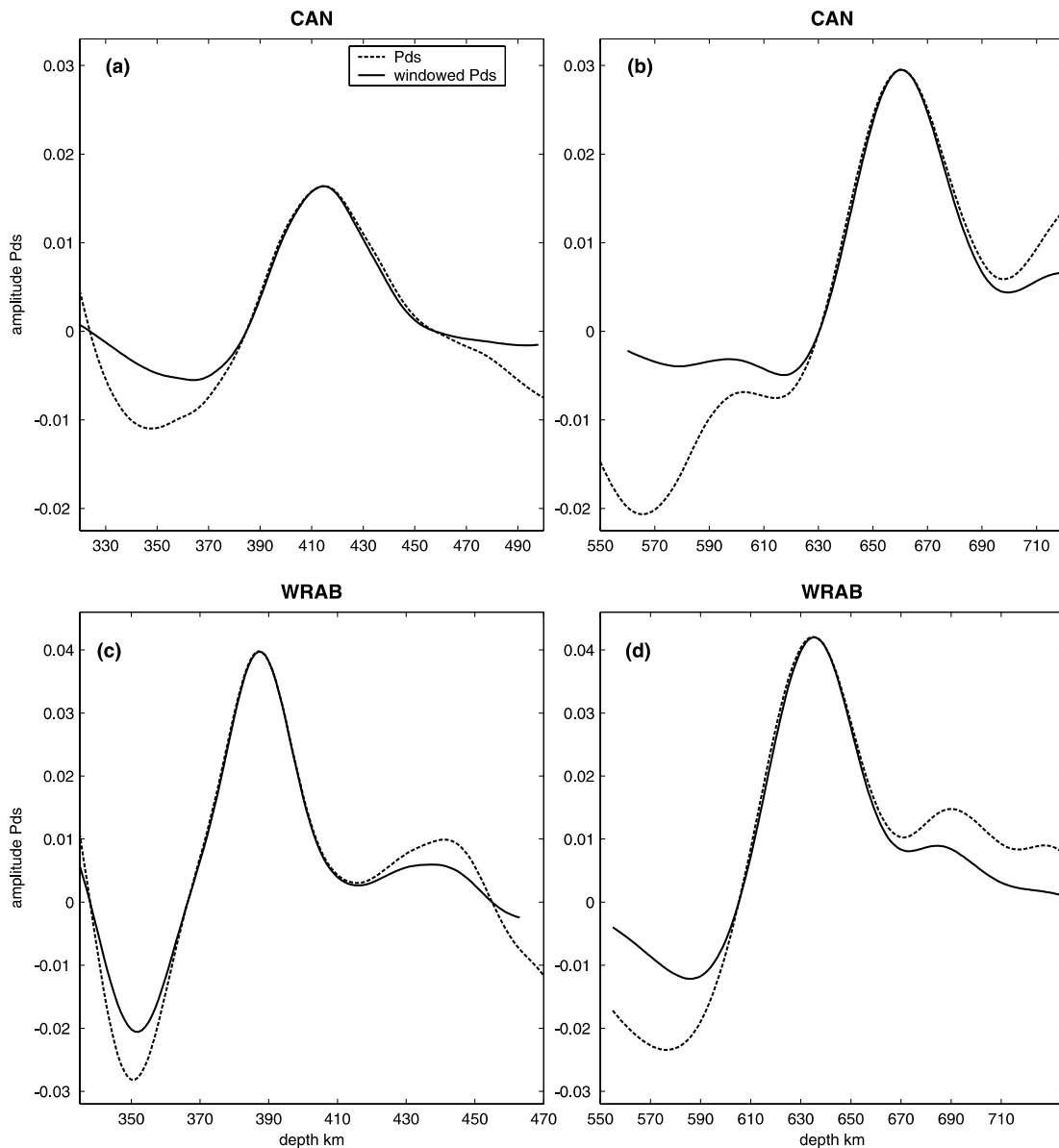
Figure 4. Imaged stacked (*Pds*) phases (dashed) at the 410-km and 660-km upper-mantle discontinuities under CAN (a and b) and WRAB (c and d). The images were obtained using the processing scheme as described in Section 3.1 on the events of CAN and WRAB, respectively. The events were deconvolved with respect to the *P* arrivals and imaged using differential traveltimes (see eq. 14) computed from a smoothed IASPEI91 reference model. The 660-km discontinuity is more pronounced in amplitude and frequency for CAN. The discontinuities for WRAB (c and d) are located at significantly shallower depth due to a different temperature under this station (Lebedev *et al.* 2002). Moreover, the frequency content is higher for both discontinuities under WRAB. Because of the ≈15 per cent velocity increase between the depths of 410 and 660 km we should expect a proportional decrease in resolution. For CAN (a and b) this decrease is not observed, while the frequency content of the 660-km discontinuity is higher. The changes in the frequency content for WRAB are consistent with the decreased resolution. To limit possible cross-talk in later analysis between different events we windowed the responses and included the windowed responses by the solid lines in the plots.

i.e. the leading-order behaviour of the converted waveforms. For CAN, the depths of the imaged upper-mantle singularities agree well with the widely accepted 410- and 660-km depth levels. We find an amplitude difference of roughly a factor of two between the 410- and 660-km depth levels under CAN, which is consistent with other observations in the literature (e.g. Xu *et al.* 2003). Images under WRAB lead to different estimates of both the depths of the transitions and the 660-to-410 amplitude ratio, presumably owing to an anomalous temperature profile in the mantle at that location (e.g. Lebedev *et al.* 2002).

3.2 Singularity characterization by matched filtering

As shown in the previous section, by using the receiver-function approach, supplemented by imaging, we gain access to the shape of the singularity, which, according to our model (see eq. 18), is related to the frequency dependence of the conversion amplitudes. In the ideal case of an infinite seismic bandwidth, the singularity order can be estimated by measuring its scaling, i.e. its response as a function of the central frequency of the source-time function. Near z_c, the wavespeed fluctuations predicted by the percolation model

lead to the following scaling (Mallat 2000) for fixed z near the singularity ($z = z_c$):

$$t_{ps} \approx \frac{d}{dz}\left(\Delta * \frac{1}{\sigma}\varphi_z^{\text{residual}}\left(\frac{\cdot}{\sigma}\right)\right) \propto \sigma^{\beta-1} \quad \text{as} \quad \sigma \to 0, \quad (19)$$

with σ proportional to the dominant wavelength/reciprocal of the spatial frequency. For fixed source-function wavelengths, the converted phases locally scale upon dilatation/compression of the depth coordinate according to $t_{ps}(rz) \propto r^{\beta-1}t_{ps}(z)$, for $r > 0$ near the singularity. For $0 < \beta < 1$, this scaling relation leads to an increasingly rapid decay of the converted amplitudes with increasing width of the coexistence region and with $\beta \to 0$.

Given the bandwidth limitation of seismic data, however, we do not have access to a wide variety of scales, rendering ineffective the multiscale analysis mentioned above. As an alternative, we use the principle of matched filtering from signal detection theory (Donoho & Johnstone 1998; Mallat 2000). We correlate the noisy bandwidth-limited image with parametrized waveform templates. By maximizing the correlation between the observed, imaged waveform and the template, we obtain estimates for the location, sharpness and dominant wavelength of the transition.

Since our aim is to estimate the exponent associated with the singularity, we construct a dictionary, D, consisting of fractional integrations of dilated B-splines (Unser & Blu 2000). The waveforms in the dictionary are defined as follows:

$$g_s^{\alpha}(z) = s^{\alpha}\frac{d^{\alpha}}{d^{\alpha}z}B\left(\frac{z}{s}\right) \quad \text{with} \quad -1 < \alpha < 0, \quad (20)$$

where B is a third-order B-spline, s the scale proportional to the dominant wavelength (frequency content), and $(d^{\alpha}/d^{\alpha}z) \cdot$ a fractional differentiation ($\alpha > 0$)/fractional integration ($\alpha < 0$) operator (Herrmann 2001) defined by

$$\frac{d^{\alpha}}{d^{\alpha}z}f(z) = (\chi^{\alpha-1} * f)(z) = \mathbf{F}^{-1}\{(j\xi)^{\alpha}\mathbf{F}f\}(z), \quad (21)$$

where $\mathbf{F}$ is the Fourier transform, $\mathbf{F}^{-1}$ the inverse Fourier transform, ξ the spatial frequency, and

$$\chi^{\alpha}(z) = \begin{cases} \dfrac{z^{\alpha}}{\Gamma(\alpha+1)} & z \geq 0 \\ 0 & z < 0 \end{cases} \quad (22)$$

a fractional power onset function with Γ denoting the Gamma function (see Herrmann 2001, and references therein). For a shear modulus fluctuation profile given by the above power functions, eq. (21) is equivalent to eq. (18). In eq. (21), the effect of the non-integer-order singularity is accounted for by the fractional integration operator. Mode conversions at singularities of the type given in eq. (22) are scale-invariant, i.e. the waveform distortions and, hence, the frequency characteristics of the converted amplitudes do not depend on the dominant wavelength of $\varphi_z^{\text{residual}}$. Note that this property is not affected by low-pass filtering.

The parametrization of the seismic waveforms is found by maximizing the correlation (i.e. minimizing the L^2-difference between observed and predicted signals) between the imaged waveforms and elements of the dictionary (Mallat 2000):

$$\{\hat{\alpha}, \hat{\sigma}\}: \quad \sup_{s \in S, \beta \in B} \langle \hat{t}_{ps}, g_s^{\beta}\rangle, \quad (23)$$

where S and B are the sets of parameters for the scale and order over which the maximization is performed, and the brackets stand for the inner product, namely $\langle f, g\rangle = \int f(z)g(z)\,dz$. Matched filtering is relatively insensitive to noise and its accuracy depends on the obtained correlation and on the suitability of the templates in the dictionary (i.e. how well the templates mimic the events, Mallat 2000).

In Fig. 5 we illustrate the effects on the modelled waveforms as a function of singularity order and dominant wavelength (of the residual source-time function/reference pulse) as predicted by the approximate convolution model of eq. (19) with the fluctuations set according to the onset function defined in eq. (22). In the absence
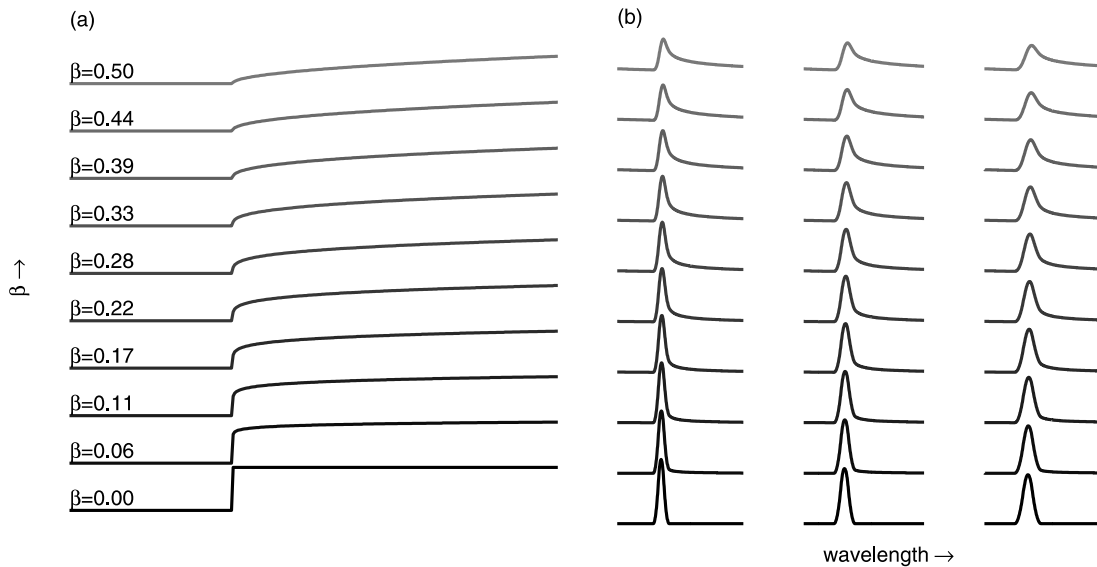

Figure 5. Onset-like singularities and their associated converted (*Pds*) phases according to the approximate convolution model given in eq. (21). (a) Increasing-order singularities with exponents $\beta = 0$ (dark shade) to $\beta = 0.5$ (light shade). Transitions of this type are scale-invariant and become sharper for decreasing β. (b) Corresponding computed converted phases (*Pds*) for increasing wavelength (from left to right). A single-scattering convolutional model was used to calculate the converted waveforms. Notice the increased asymmetry for increasing β, irrespective of the central frequency/wavelength of the reference pulse.
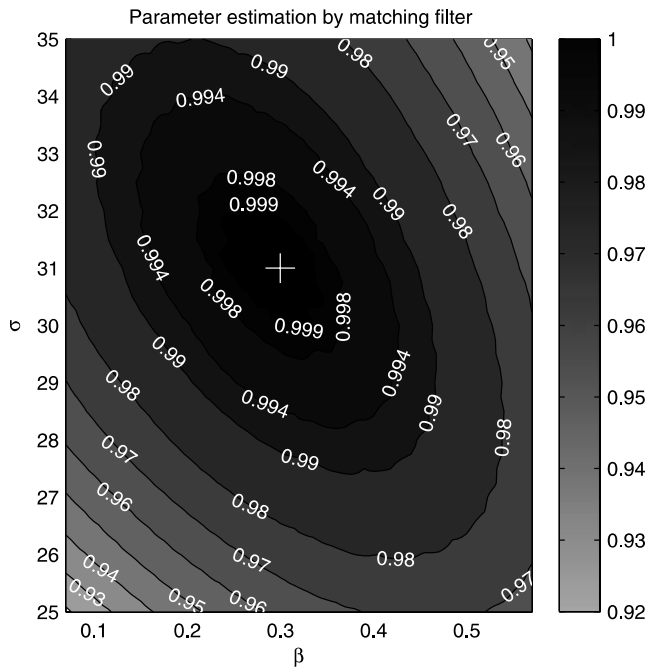
Figure 6. Singularities are estimated by finding the best correlation between the parametrized waveform (solid lines in Fig. 7) and the windowed *Pds* (dashed lines in Fig. 4). Varying the scale and order parameters leads to an ellipsoidal convex correlation function with a unique maximum (indicated by the white '+' symbol), as can be observed in this figure where the 410-km singularity under CAN is analysed. The estimated exponents are $\beta_{410} = 0.30$, $\beta_{660} = 0.27$ for CAN and $\beta_{410} = 0.29$, $\beta_{660} = 0.33$ for WRAB. Differences in depth for the singularities and the width of the transition zone are mainly due to differences in temperature (Lebedev *et al.* 2002) in the mantle underneath these stations.

of dispersion, the scale is a measure of stacking coherence, as well as an estimate of a possible finite-size effect, which gives rise to a smoothing of the singularity in eq. (22).

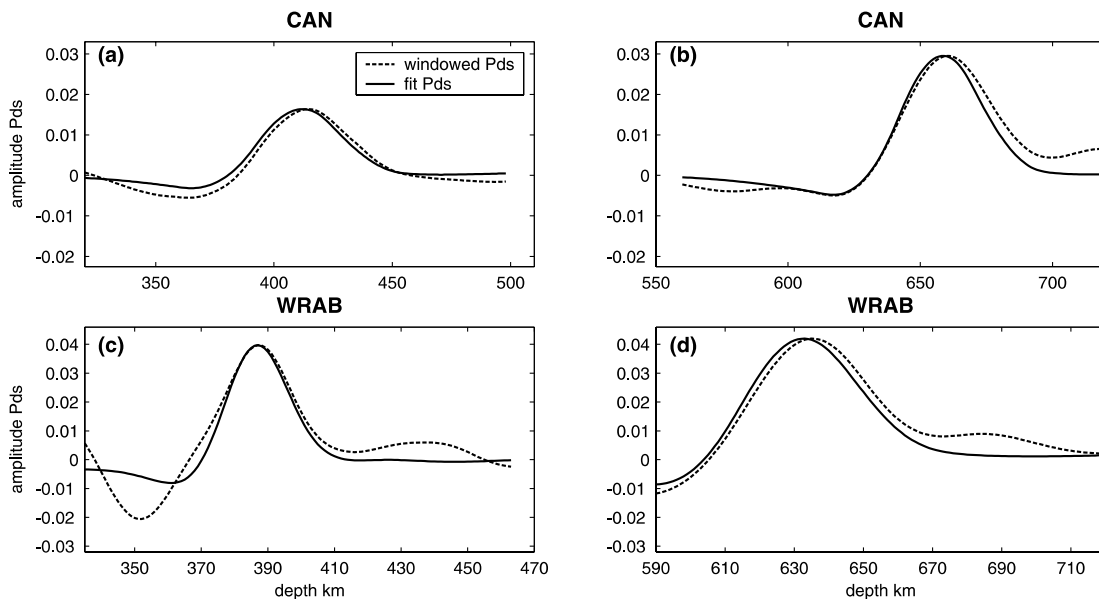In Figs 6 and 7 we show our matched-filtering findings for the two Australian stations, CAN (geoscope) and WRAB (IRIS). In the case of the 410-km transition under CAN, Fig. 6 shows a well-defined ellipsoid (no local minima) for the correlation function (see eq. 23). There is clearly one single maximum, although 'leakage' between the two parameters (i.e. singularity order and scale) does occur. Good fits were obtained between the imaged singularities and the selected parametric waveforms. Estimates for the βs lie in the range [0.25–0.35] for both stations. Specifically, we found $\beta_{410} = 0.30$, $\beta_{660} = 0.27$ for CAN, and $\beta_{410} = 0.29$, $\beta_{660} = 0.33$ for WRAB. We reduced possible cross-talk between the different events by applying spatial windows, centred near the approximate locations of the singularities (see the red lines in Fig. 4, which depict the waveforms after applying the window). Since the primary interest of this paper is gaining access to the exponent β, the scale is of lesser interest and we will limit ourselves to qualitative statements only. After accounting for resolution changes resulting from the increase in shear-wave velocity with depth (decreasing the resolution), we find similar scale estimates for the 410- and 660-km singularities for WRAB. For CAN, the 660-km singularity is more pronounced in amplitude as well as in frequency content/sharpness, which is reflected in the estimates for the exponent. These results are consistent with findings published in the literature. For example, Xu *et al.* (2003) reported a ratio in amplitudes between the 410- and 660-km singularities of approximately 2 for $P'P'$ precursors.

4 SIMULATION OF CONVERTED WAVES

The next step is to simulate the mode conversions of the elastic waves at the 410- and 660-km singularities. For this purpose, we need to specify the parameters of the model described in Section 2. As already explained, we use the values of the exponent β inferred from seismic data in Section 3. We also assume that the coexistence regions extend from 320 to 500 km for the 410- and from 550 to 750 km for the 660-km phase transition. Our choice was inspired by fig. 1 in Bina (1991), except for the deepest boundary, which we fixed somewhat arbitrarily. Since we do not want to link our transition model to a specific mineralogy, we assign wavespeed and density values typical of plausible mineral groups. Thus, we consider the
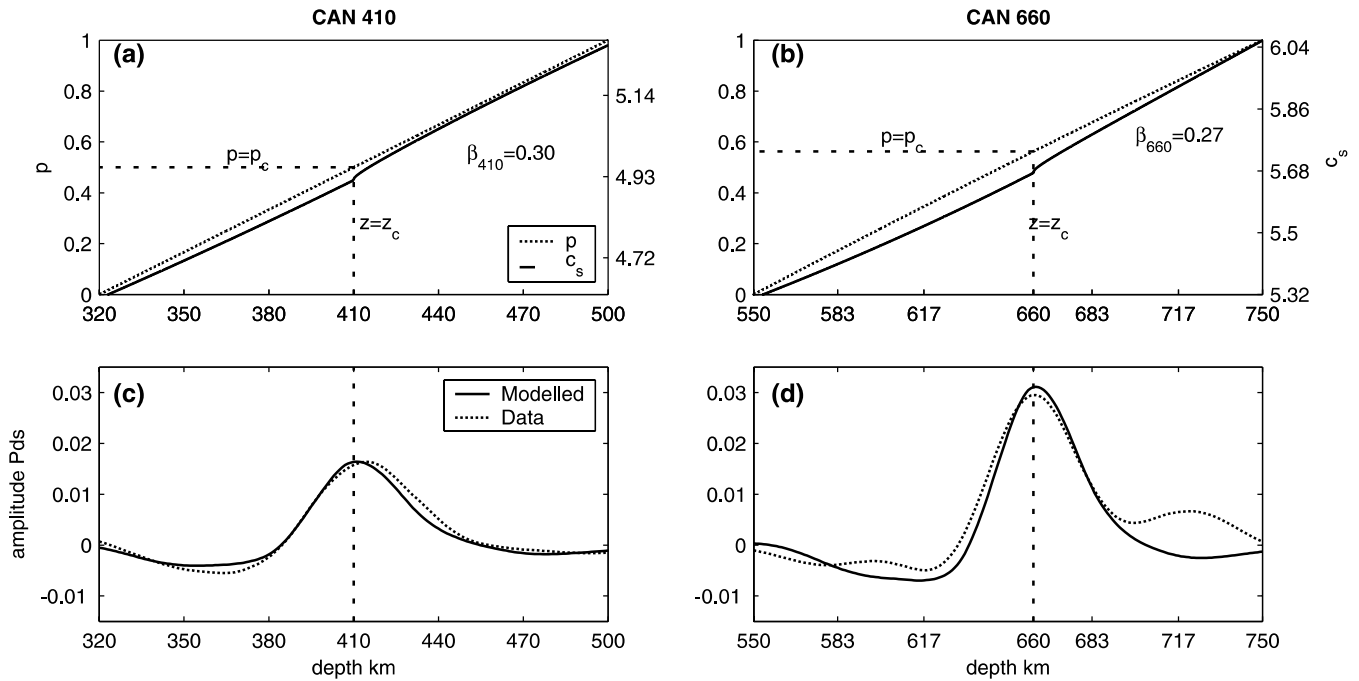

Figure 7. Comparison between the imaged and matched parametric waveforms. The parametric waveforms (solid lines) are defined in terms of the estimated exponents listed in the caption of Fig. 6.

Figure 8. Comparison between images of observed *Pds* phases and images calculated from forward-modelled synthetics. (a) and (b) 410/660-transition models as predicted by the percolation model with exponents constrained by the parameter estimates depicted in Fig. 1. The shear wavespeed profiles (solid lines) contain onset-like singularities, irrespective of the gradients in the volume fraction (dashed lines) for the HP material. The dashed lines indicate the critical volume fraction and corresponding depth. (c) and (d) Windowed, imaged *Pds* phases (dashed lines) for the 410- and 660-km discontinuities under CAN, and corresponding images (solid lines), obtained after forward modelling in a transition zone predicted by percolation consisting of two non-overlapping coexistence regions with exponents set according the estimates. The seismic synthetics were created using an elastic transfer-matrix method that includes multiple scattering and mode conversions. We subsequently imaged these synthetics using a smoothed velocity model. The waveforms of the synthetic images agree well with those of the imaged *Pds* phases under CAN.

olivine/orthopyroxene group as for the LP phase for the 410-km transition, the broad group covering β- and γ-spinel, Na- and Mg-majorite, and garnet as HP for the 410- and LP for the 660-km transition, and perovskite as HP for the 660-km transition. Specifically, we choose $V_p = 8.62$ km s^{-1}, $V_s = 4.71$ km s^{-1} and $\rho = 3.46$ g cm^{-3} for the LP phase and $V_p = 9.45$ km s^{-1}, $V_s = 5.19$ km s^{-1} and $\rho = 3.76$ g cm^{-3} for the HP phase at the depth of 410 km, and $V_p = 9.98$ km s^{-1}, $V_s = 5.39$ km s^{-1} and $\rho = 3.93$ g cm^{-3} for the LP phase and $V_p = 10.83$ km s^{-1}, $V_s = 5.96$ km s^{-1} and $\rho = 4.19$ g cm^{-3} for the HP phase at 660 km. These values as well as the depth gradients were taken from figs 3-7 and 3-8 of Anderson (1989). The corresponding values calculated for the mixture using eqs (9)–(11) are $V_p = 8.99$ km s^{-1}, $V_s = 4.92$ km s^{-1} and $\rho = 3.61$ g cm^{-3} at $z = 410$ km, and, $V_p = 10.40$ km s^{-1}, $V_s = 5.67$ km s^{-1} and $\rho = 4.08$ g cm^{-3} at $z = 660$ km (consistent with PREM;, Dziewonski & Anderson 1981). As will be shown next, this model leads to a good agreement with seismic observations from converted phases. We also tested eqs (3)–(5) (i.e. isotropic case), but they did not yield sufficiently large singularity magnitudes to produce waveforms with amplitudes matching the observations.

Given the above model, we define an isotropic finely layered medium using a discretization of eqs (9)–(11) and assuming a layer thickness of 10 m, well below the dominant wavelength. For this medium, we compute the transmission response, including all multiples and mode conversions, using a ray-parameter domain ($[\tau - p]$-domain) elastic transfer matrix/reflectivity method (Kennett 2001) for the same ray parameters as the recorded events. We then process the modelled broadband response according to the

imaging scheme described in Section 3.1. In order to make a comparison between the modelled response and the images we finally convolve the imaged synthetic response with a bandpass filter whose frequency characteristics are similar to those of the estimated residual source-time function. As a final step, we apply the same smoothing filter as we used to improve the coherence of the imaged recorded data. The results for the two stations are depicted in Fig. 8. Comparison of the modelled and measured images shows good agreement between the waveforms yielded by our model and those obtained from the seismic events recorded at CAN. The waveform and, hence, the frequency-dependent amplitudes are captured well by our parametrization, i.e. by the percolation model proposed here. Finally, note that we did not need significant adjusting to match the amplitudes at the peaks, which suggests that the magnitude of the singularity predicted by the percolation model is approximately correct.

5 DISCUSSION AND CONCLUSIONS

In this paper, we propose a new model for the structure of the upper-mantle transition zone that provides an alternative explanation for the seismic response of the upper-mantle phase transitions as well as the anomalous gradients observed in the entire region between them. Our main goal was to devise a plausible model, based on solid physical arguments, that not only explains the seismic observations (for example the frequency dependence and scaling of the amplitudes of the converted waves), but also provides insight into

the intricate interplay between changes in the mineralogy and their physical manifestation in the elastic moduli.

Major support of our percolation model is provided by (1) theoretical and experimental results in the field of mechanical engineering demonstrating that the elastic moduli of a binary mixture are controlled by the percolation properties of the strongest phase (e.g. de Gennes 1976; Ledbetter *et al.* 1984; Gai *et al.* 1984; Deptuck *et al.* 1985; Turusov *et al.* 1986; Marion & Nur 1989; Favier *et al.* 1997; Novikov *et al.* 2001; Saidi *et al.* 2003), (2) the identification of singularities at the expected depths and the quantitative determination of the exponents from seismic data, and (3) the good fit obtained between the synthetic and receiver-function images. However, the limited spatial extent of this study does not allow us to make a global statement on the order of the singularities, which may vary regionally.

For a brief discussion of the implications of the percolation model, we give below a list of additional remarks and predictions.

(1) We do not invoke a singular behaviour of the phase transition itself, which is consistent with published experimental mineralogy results.

(2) The mixing law for density is smooth because density is an additive parameter not affected by percolation. Despite the relative insensitivity of converted phases to density, we attempted to invert seismic data for density and shear wavespeed. The results showed a negligible density response, providing additional support to our model.

(3) The model implies significant scattering by inclusion clusters (see also Perlovsky 1986, 1991). This prediction is confirmed by the presence of incoherent events in the observed transverse component in the region between the two discontinuities. The power spectra of these fluctuations for both radial and transverse components are nearly identical power-law functions of the wavelength, and, therefore, of inclusion cluster size. This behaviour is consistent with cluster number statistics from percolation theory. Moreover, these predictions are supported by recent results on scattering at upper-mantle heterogeneities (e.g. Thybo *et al.* 2003). The heterogeneity we predict is a consequence of cluster formation, while the discontinuity itself is related to the formation of a spanning cluster.

(4) To account for the observed seismic amplitudes, we considered horizontally oriented non-spherical inclusions with very small shape factors, giving rise to a transverse isotropic structure with a vertical symmetry axis. In the future, it would be interesting to see how this prediction fits into models of the anisotropy in the upper mantle.

(5) Because our model relies on singularities, there is no need to assume very narrow coexistence regions. In fact, broad coexistence regions are consistent with the observation of anomalous gradients across the entire transition zone (e.g. Dziewonski & Anderson 1981; Anderson 1989; Karki *et al.* 2001; Sinogeikin & Bass 2002). This assumption is not incompatible with laboratory results, which have shown that some plausible mineral systems do transform gradually with depth (for example eclogite to garnetite, and garnet-majorite to perovskite; see Anderson 1989; Bina 1991; Helffrich & Wood 2002). We suggest that many features could be more readily explained by considering that the mantle has a complex composition. For example, in the case of the 410-km singularity, we could speculate that a major component of the mantle would be eclogite mixed with enough olivine to ensure that the percolation threshold is situated at a depth very near 410 km (a similar structure can be envisioned for the 660-km singularity).

(6) The scale invariance (see eq. 19 and ensuing discussion) resulting from the percolation model allows two predictions. (a) The frequency-dependent amplitude behaviour of the waveforms of the converted phases is independent of the seismic wavelength of the incident *P* wave. (b) Rescaling of the conversion amplitude strongly depends on the width of the mixing zone (for example, for an exponent of $\beta = 0.30$ the maximum amplitude decreases by a factor of $2^{\beta-1} = 2^{-0.7}$ when the width is doubled). This rescaling argument can be used to explain the difference between the observed peak amplitudes for the 410- and 660-km singularities. It is also consistent with the differences in predicted thickness for the phase transitions based on mineralogical arguments. For example, if we fix the thickness of the 660-km singularity to $\approx$3 km (which is consistent with reported thicknesses in the literature) then we need a thickness of approximately 8 km $\left(\left(\frac{1}{2}\right)^{\frac{1}{\beta-1} = \frac{1}{-0.7}} \times 3 \approx 8\right)$ for the 410-km singularity to explain the difference of a factor of 2 in the observed amplitudes for the 410- and 660-km singularities (e.g. Xu *et al.* 2003). This prediction is consistent with findings for the average thickness of the 410-km singularity and significantly exceeds differences in amplitude caused by differences in the wavelength related to the increase in compressional wavespeed between the depths of the 410- and 660-km singularities. Moreover, our predictions for the observed waveforms and amplitudes are a direct consequences of fractional-order transitions and do not require subwavelength combinations of first- and zero-order discontinuities to explain differences between the 410- and 660-km phase transitions (Xu *et al.* 2003).

In conclusion, our model can help to further constrain the physics and fine structure of the upper-mantle transition zone. For example, seismic events between the singularities (for example the '525-km discontinuity') may be associated with gradient jumps at the ends of the coexistence regions (i.e. from the gradient due to phase mixing to that caused by pressure dependence). These latter discontinuities are of first order and, hence, less sharp, which explains the fact that the '525-discontinuities' are not as frequently observed as the 410- and 660-km transitions. Our method could be applied to data recorded at seismological stations in other parts of the Earth. Comparing the results obtained at these different positions on the Earth may help to delineate lateral variations in the transition zone. Finally, the ideas presented here can also be applied to other interfaces in the Earth.

REFERENCES

Abramovich, F. & Silverman, B., 1998. The vaguelette-wavelet decomposition approaches to statistical inverse problems, *Biometrika,* **85,** 115–129.

Akaogi, M., Navrotsky, A., Yagi, T. & Akimoto, S., 1987. Pyroxene-garnet transformation: thermochemistry and elasticity of garnet solid solutions, and application to a pyrolite mantle, in, *High Pressure Research in Mineral Physics,* pp. 251–260, eds Manghani, M.H. & Syono, Y., Am. Geophys. Union, Washington, DC.

Anderson, D.L., 1989. *Theory of the Earth,* Blackwell Scientific Publications, London.

Anderson, D.L. & Bass, J.D., 1986. The transition region of the Earth's upper mantle, *Nature,* **320,** 321–328.

Bass, J.D. & Anderson, D.L., 1984. Composition of the upper mantle: geophysical tests of two petrological model, *Geophys. Res. Lett.,* **11,** 229–233.

Benveniste, Y., 1987. A new approach to the application of Mori-Tanaka's theory in composite materials, *Mech. Mater.,* **6,** 147–157.

Bina, C.R., 1991. Mantle discontinuities, U.S. Natl. Rep. Int. Union Geodes. Geophys. 1987–1990, *Rev. Geophys.,* **29,** 783–793.

Bina, C.R. & Wood, B.J., 1984. The eclogite to garnerite transition - experimental and thermodynamic constraints, *Geophys. Res. Lett.,* **11,** 955–958.

Chevrot, S., Vinnik, L. & Montagner, J.P., 1999. Global scale analysis of the mantle *Pds* phases, *J. geophys. Res.,* **104,** 20 203–20 219.

Claerbout, J.F., 1971. Toward a unified theory of reflector mapping, *Geophysics,* **36,** 467–481.

Cox, H., 2002. Seismic Discontinuities and Order Estimation Using Wavelets: A Receiver Function Approach, *MSc thesis,* MIT.

de Gennes, P.-G., 1976. On a relation between percolation theory and the elasticity of gels, *J. Physique Lett.,* **37,** L1–L2.

Deptuck, D., Harrison, J.P. & Zawadski, P., 1985. Measurement of elasticity and conductivity of a three-dimensional percolation system, *Phys. Rev. Lett.,* **54,** 913–916.

Donoho, D. & Johnstone, I., 1998. Minimax estimation via wavelet shrinkage, *Ann. Statist,* **26,** 879–921.

Dziewonski, A. & Anderson, D.L., 1981. Preliminary reference earth model, *Phys. Earth planet. Inter.,* **25,** 297–356.

Eshelby, J.D., 1957. The determination of the elastic field of an ellipsoidal inclusion, and related problems, *Proc. R. Soc. A,* **241,** 376–396.

Favier, V., Dendeviel, R., Canova, G., Cavaille, J.Y. & Gilormini, P., 1997. Simulation and modeling of three-dimensional percolating structures: case of latex matrix reinforced by a network of cellulose fibers, *Acta Mater.,* **45,** 1557–1565.

Gaherty, J., Wang, Y., Jordan, T. & Weidner, D., 1999. Testing plausible upper-mantle compositions using fine-scale models of the 410-km discontinuity, *Geophys. Res. Lett.,* **26,** 1641–1644.

Gai, M.I., Manevich, L.I. & Oshmyan, V.G., 1984. Percolation effects in mechanical systems, *Dokl. Akad. Nauk SSSR,* **276,** 1389–1391(in Russian).

Grand, S.P., Van der Hilst, R.D. & Widiyantoro, S., 1997. High resolution global tomography: a snapshot of convection in the Earth, *Geol. Soc. Am. TODAY,* **7,** 1–7.

Gu, Y., Dziewonski, A.M. & Agee, C.B., 1997. Global de-correlation of the topography of transition zone discontinuities, *Earth planet. Sci. Lett.,* **157,** 57–67.

Gurrola, H. & Minster, J., 1998. Thickness estimates of the upper-mantle transition zone from bootstrapped velocity spectrum stacks of receiver functions, *Geophys. J. Int.,* **133,** 31–43.

Hashin, Z. & Shtrikman, S., 1962. On some variational principles in anisotropic and nonhomogeneous elasticity, *J. Mech. Phys. Solids,* **10,** 335–342.

Helffrich, G.R. & Wood, B.J., 2002. The Earth's mantle, *Nature,* **412,** 501–507.

Herrmann, F.J., 2001. Singularity characterization by monoscale analysis, *J. appl. Comput. harmon. Anal.,* **11,** 64–88.

Herrmann, F.J., Lyons, W. & Stark, C., 2001. Seismic facies characterization by monoscale analysis, *Geophys. Res. Lett.,* **28,** 3781–3784.

Isichenko, M.B., 1992. Percolation, statistical topography, and transport in random media, *Rev. Mod. Phys.,* **64,** 961–1043.

Kaganova, I.M. & Roitburd, A.L., 1988. Equilibrium between elastically-interacting phases, *Sov. Phys. JEPT,* **67,** 1173–1183.

Karki, B.B., Stixrude, L. & Wentzcovitch, R.M., 2001. High-pressure elastic properties of major materials of Earth's mantle from first principles, *Rev. Geophys.,* **39,** 507–534.

Kennett, B.L.N., 2001. *The Seismic Wavefield,* **Vol. I**; Cambridge Press, London.

Kennett, B.L.N. & Engdahl, E.R., 1991. Traveltimes for global earthquake location and phase identification, *Geophys. J. Int.,* **105,** 429–465.

Lebedev, S., Chevrot, S. & van der Hilst, R., 2002. Seismic evidence for olivine phase changes at the 410- and 660-kilometer discontinuities, *Science,* **296,** 1300–1302.

Ledbetter, H.M., Dutta, S.K. & Kriz, R.D., 1984. Elastic constants of an anisotropic nonhomogeneous particle-reinforced composite, *Acta Metall.,* **32,** 2225–2231.

Luo, H.A. & Weng, G.J., 1987. On Eshelby's inclusion problem in a three-phase spherically concentric solid and a modification of Mori-Tanaka's method, *Mech. Mater.,* **6,** 347–361.

Mallat, S.G., 2000. *A Wavelet Tour of Signal Processing,* Academic Press, London.

Marion, D. & Nur, A., 1989. Percolation of electrical and elastic properties of granular materials at the transition from a suspension to a loose packing, *Physica A,* **157,** 575–579.

Mori, T. & Tanaka, K., 1973. Average stress in matrix and average elastic energy of materials with misfitting inclusions, *Acta Metall.,* **21,** 571–574.

Mura, T., 1982. *Micromechanics of Defects in Solids,* Martinus Nijhoff Publishers, Boston.

Neelamani, R., Choi, H. & Baraniuk, R.G., 2004. ForWaRD: Fourier-Wavelet Regularized Deconvolution for ill-conditioned systems, *IEEE Trans. Signal Processing,* **52,** 418–433.

Novikov, V.V., Wojciechowski, K.W., Belov, D.V. & Privalko, V.P., 2001. Elastic properties of inhomogeneous media with chaotic structure, *Phys. Rev. E,* **63,** 036120(1–7).

Paulssen, H., 1988. Evidence for a sharp 670-km discontinuity as inferred from P-to-S converted waves, *J. geophys. Res.,* **93,** 10 489–10 500.

Perlovsky, L.I., 1986. Scattering of seismic waves by shear modulus fluctuation due to rigid-non rigid phase transition, *Boll. Geofis. Teorica & Appl.,* **28,** 3–13.

Perlovsky, L.I., 1991. Acoustic critical opalescence of the transitional under-ice layer in the Arctic, *Boll. Geofis. Teorica & Appl.,* **33,** 237–256.

Petersen, N., Vinnik, L., Kosarev, G., Kind, R., Oreshin, S. & Stammler, K., 1993. Sharpness of the mantle discontinuities, *Geophys. Res. Let.,* **20,** 859–862.

Revenaugh, J. & Jordan, T.H., 1991. Mantle layering from ScS reverberations: 2. The transition zone, *J. geophys. Res.,* **96,** 19 763–19 780.

Roux, S. & Guyon, E., 1985. Mechanical percolation: a small beam lattice study, *J. Physique Lett.,* **46,** L999–L1004.

Sahimi, M. & Mukhopadhyay, S., 1996. Scaling properties of a percolation model with long-range correlations, *Phys. Rev. E,* **54,** 3870–3880.

Saidi, F., Bernabé, Y. & Reuschlé, T., 2003. The mechanical behaviour of synthetic, poorly consolidated granular rock under uniaxial compression, *Tectonophysics,* **370,** 105–120.

Schjodt-Thomsen, J. & Pyrz, R., 2001. The Mori-Tanaka stiffness tensor: diagonal symmetry, complex fibre orientations and non-dilute volume fractions, *Mech. Mater.,* **33,** 531–544.

Shearer, P.M., 1990. Seismic imaging of upper-mantle structure with new evidence for a 520-km discontinuity, *Nature,* **344,** 121–126.

Shearer, P.M. & Flanagan, M., 1999. Seismic velocity and density jumps across the 410- and 660-kilometer discontinuities, *Science,* **284,** 1545–1548.

Sinogeikin, S.V. & Bass, J.D., 2002. Elasticity of majorite and a majorite-pyrope solid solution to high pressure: implications for the transition zone, *Geophys. Res. Lett.,* **29,** doi:10.1029/2001GL013937.

Stauffer, D. & Aharony, A., 1992. *Introduction to Percolation Theory,* p. 124, Taylor and Francis, London.

Thomsen, L., 1986. Weak elastic anisotropy, *Geophysics,* **51,** 1954–1966.

Thybo, H., Nielsen, L. & Perchuck, E., 2003. Seismic scattering at the top of the mantle transition zone, *Earth planet. Sci. Lett.,* **216,** 259–269.

Turusov, R.A., Gai, M.I., Manevich, L.I., Oshmyan, V.G., Zelenskii, E.S., Sluyaeva, Z.P. & Sochnev, V.I., 1986. Experimental study of the mechanical properties of a composite on the basis of percolation approach, *Dokl. Akad. Nauk. SSR,* **291,** 850–853.

Unser, U. & Blu, T., 2000. Fractional splines and wavelets, *SIAM Rev.,* **42,** 43–67.

Weidner, D.J. & Wang, Y., 2000. Phase transformations: implications for mantle structure, in *Earth's Deep Interior: Mineral Physics and Tomography From the Atomic to the Global Scale,* pp. 215–235, AGU Geophys. Monograph, Washington, DC.

Xu, F., Vidale, J. & Earle, E., 2003. Survey of precursors to P'P': Fine structure of mantle discontinuities, *J. geophys. Res.,* **108,** 2024, doi:10.1029/2001JB000817.